

A multi-frequency sparse hemispherical ultrasound phased array for microbubble-mediated transcranial therapy and simultaneous cavitation mapping

Lulu Deng^{1,4}, Meaghan A O'Reilly^{1,2}, Ryan M Jones^{1,2},
Ran An¹ and Kullervo Hynynen^{1,2,3}

¹ Physical Sciences Platform, Sunnybrook Research Institute, Toronto, ON M4N 3M5, Canada

² Department of Medical Biophysics, University of Toronto, Toronto, ON M5G 1L7, Canada

³ Institute of Biomaterials and Biomedical Engineering, University of Toronto, Toronto, ON M5S 3G9, Canada

E-mail: lldeng@sri.utoronto.ca

Received 28 August 2016

Accepted for publication 18 October 2016

Published 15 November 2016



CrossMark

Abstract

Focused ultrasound (FUS) phased arrays show promise for non-invasive brain therapy. However, the majority of them are limited to a single transmit/receive frequency and therefore lack the versatility to expose and monitor the treatment volume. Multi-frequency arrays could offer variable transmit focal sizes under a fixed aperture, and detect different spectral content on receive for imaging purposes. Here, a three-frequency (306, 612, and 1224 kHz) sparse hemispherical ultrasound phased array (31.8 cm aperture; 128 transducer modules) was constructed and evaluated for microbubble-mediated transcranial therapy and simultaneous cavitation mapping. The array is able to perform effective electronic beam steering over a volume spanning (−40, 40) and (−30, 50) mm in the lateral and axial directions, respectively. The focal size at the geometric center is approximately 0.9 (2.1) mm, 1.7 (3.9) mm, and 3.1 (6.5) mm in lateral (axial) pressure full width at half maximum (FWHM) at 1224, 612, and 306 kHz, respectively. The array was also found capable of dual-frequency excitation and simultaneous multi-foci sonication, which enables the future exploration of more complex exposure strategies. Passive acoustic mapping of dilute microbubble clouds demonstrated that the point spread function of the receive array has a lateral (axial) intensity FWHM between 0.8–3.5 mm (1.7–11.7 mm) over a volume spanning

⁴ Author to whom any correspondence should be addressed.

(−25, 25) mm in both the lateral and axial directions, depending on the transmit/receive frequency combination and the imaging location. The device enabled both half and second harmonic imaging through the intact skull, which may be useful for improving the contrast-to-tissue ratio or imaging resolution, respectively. Preliminary *in vivo* experiments demonstrated the system's ability to induce blood–brain barrier opening and simultaneously spatially map microbubble cavitation activity in a rat model. This work presents a tool to investigate optimal strategies for non-thermal FUS brain therapy and concurrent microbubble cavitation monitoring through the availability of multiple frequencies.

Keywords: transcranial ultrasound, multi-frequency phased array, focused ultrasound therapy, passive cavitation mapping

(Some figures may appear in colour only in the online journal)

Introduction

Focused ultrasound (FUS) therapy is currently being investigated for various transcranial applications, including thermal ablation for the treatment of brain tumors (McDannold *et al* 2010, Coluccia *et al* 2014) and other neurological disorders such as essential tremor (Elias *et al* 2013, Lipsman *et al* 2013, Chang *et al* 2014), Parkinson's disease (Fry and Fry 1960, Magara *et al* 2014), and chronic neuropathic pain (Martin *et al* 2009, Jeanmonod *et al* 2012), sonothrombolysis for stroke therapy (Alexandrov *et al* 2004, Burgess *et al* 2012), as well as ultrasound-mediated blood–brain barrier (BBB) opening (Hynynen *et al* 2001, Choi *et al* 2007) for targeted drug delivery to the central nervous system (Kinoshita *et al* 2006, Liu *et al* 2010, Aryal *et al* 2013). FUS brain therapy offers many advantages as a potential treatment option, as the procedures are non-invasive, non-ionizing and can target deep-seated tissues that are otherwise difficult to treat. As a result, FUS serves as a favorable alternative to conventional therapeutic methods involving either the removal of a piece of skull bone (Chi *et al* 1996, Lapchak and Araujo 2007, Nau *et al* 2010, Riordan and Tovar-Spinoza 2014), or the use of ionizing radiation (Matsunaga *et al* 2010).

Two major challenges faced by transcranial FUS therapy involve overcoming the aberrating effects induced by the skull bone in order to generate an adequate focus in the brain (Fry and Barger 1978) and mitigating the effects of skull heating caused by the highly attenuating nature of bone (Fry 1977). At the turn of the century, it was discovered that non-invasive aberration correction can be achieved through knowledge of skull density and thickness maps obtained from pre-operative CT images (Clement and Hynynen 2002a, Aubry *et al* 2003), and that the use of a large-aperture multi-element phased array geometrically minimizes skull heating by maximizing the penetration area on the skull surface (Hynynen and Jolesz 1998, Sun and Hynynen 1999, Clement *et al* 2000b). The feasibility of using hemispherical phased array transducers to perform FUS therapy in the brain has since been demonstrated in several pre-clinical (Clement *et al* 2000a, Hynynen *et al* 2004, 2006, Pernot *et al* 2007, Tanter *et al* 2007, Liu *et al* 2008, Marquet *et al* 2013) and clinical (McDannold *et al* 2010, Elias *et al* 2013, Lipsman *et al* 2013, Chang *et al* 2014) studies. Since the first transcranial phased array was designed (Clement *et al* 2000a), arrays with relatively high transducer element counts (up to 1372 in the array described in Song and Hynynen (2010)) have been manufactured and, more recently, systems with two (Liu *et al* 2014) or more (Lin *et al* 2014) transmit frequencies have been developed.

To ensure the safety and accuracy of transcranial FUS therapy, magnetic resonance imaging (MRI) thermometry (McDannold 2005), which exploits the temperature dependence of the magnetic properties of water (Hindman 1966), can be used to monitor thermal-based therapies (McDannold *et al* 2010, Elias *et al* 2013, Lipsman *et al* 2013). However, non-thermal brain treatments, such as FUS-induced BBB opening (Hynynen *et al* 2001), are more challenging to monitor via MRI. Recent studies have demonstrated that passive imaging of microbubble activity with an array of detectors (Salgaonkar *et al* 2009, Gâteau *et al* 2010, Gyongy and Coussios 2010) is a promising method for monitoring ultrasound-mediated BBB opening procedures (Arvanitis *et al* 2013, O'Reilly *et al* 2014, Jones *et al* 2015), as spectral characteristics of the acoustic emissions occurring during such treatments have been linked with biological outcome (McDannold *et al* 2006, Tung *et al* 2010, Arvanitis *et al* 2012, O'Reilly and Hynynen 2012). For example, in a recent study by Arvanitis *et al* a one-dimensional (1D) linear diagnostic ultrasound array was integrated within a commercial clinical MRI-guided brain therapy device to receive ultrasound signals and spatially map cavitation activity in two-dimensions during BBB opening in non-human primates (Arvanitis *et al* 2013). The spatial information afforded by small-aperture 1D arrays during passive imaging is fundamentally limited, though this approach can be refined by placing the receive elements on a large hemispherical shell (Jones *et al* 2013). This method provides several major improvements: first, both the imaging resolution and receive sensitivity improve with increasing array aperture during passive beamforming (Norton and Won 2000), and second, it allows for three-dimensional (3D) passive imaging, which is not possible with a 1D array without mechanical translation or rotation of the device. Recently, our group has integrated a 128-element hemispherical sparse receiver array with a central frequency of 612 kHz into an existing hemispherical phased array prototype (30 cm diameter) with a fundamental driving frequency of 306 kHz (Song and Hynynen 2010). We have employed the dual-mode system for FUS-induced BBB opening with simultaneous 3D cavitation mapping through *ex vivo* human skulls (O'Reilly *et al* 2014) using CT-based aberration corrections (Jones *et al* 2015) and for studies investigating aberration correction techniques (Jones and Hynynen 2016), as well as for transcranial imaging beyond the diffraction limit (O'Reilly and Hynynen 2013). However, this device is limited to a single combination of transmit and receive frequencies; it is therefore only capable of imaging bubble activity within a narrow bandwidth around the second harmonic, and has a fixed focal size on both transmit and receive mode.

In the current study, a three-frequency transmit/receive hemispherical sparse ultrasound phased array is presented. The array consists of 128 independent modules, each of which contains three concentric cylindrical narrow-band transmit/receive transducer elements with fundamental frequencies of 306, 612, and 1224 kHz, respectively, allowing for up to six combinations of transmit and receive frequencies. This design improves upon previously developed FUS brain systems in several ways. On the transmit side, the availability of multiple driving frequencies allows for variable transmit focal volume sizes from the same device, and enables simultaneous multi-frequency excitation. This latter point is of interest as dual-frequency sonications have been shown to enhance sonochemical effects (Umemura *et al* 1996), selectively promote cavitation activity at the focus while suppressing its occurrence in surrounding regions (Sokka *et al* 2005), and augment ultrasound-mediated BBB opening (Liu *et al* 2014) compared to mono-frequency exposures. On the receive side, the ability to capture microbubble emissions at both the half- and second-harmonic frequencies offers increased flexibility from an imaging and treatment control standpoint. For instance, second-harmonic imaging is an attractive option since spatial resolution improves with increasing source frequency during passive imaging (Norton and Won 2000). Additionally, second-harmonic imaging has been shown to improve the detection of nonlinear microbubble scattering from

within vessels (Burns *et al* 1994, Pasovic *et al* 2011), and therefore has potential application in ultrasound-based vascular mapping (Mulvagh *et al* 1996, O'Reilly and Hynynen 2013). On the other hand, half-harmonic imaging could be employed to enhance the contrast-to-tissue ratio (Shankar *et al* 1998), and has the advantage of reduced signal attenuation through the human cranial bone at lower source frequencies (Fry 1977). Furthermore, signals received at both the half-harmonic (O'Reilly and Hynynen 2012) and second-harmonic (Arvanitis *et al* 2012) frequencies have been proposed for acoustic emissions-based feedback controllers for ultrasound-mediated BBB opening, and this device could enable a direct comparison between these two strategies. Thus, the array presented in this study provides a tool for exploring both the advantages of selectable mono-frequency or multi-frequency exposures on transmit, as well as the merits of frequency-selective passive cavitation imaging on receive.

Materials and methods

Phased array construction

The base frame of the array was a Lucite hemispherical dome with an inner diameter of 31.8 cm and a wall thickness of 0.635 cm (Global Plastic Services, Calais, Maine, USA). 128 transducer modules were integrated within the dome as shown in figure 1(a). An illustration of the cross-sectional view of one module is shown in figure 1(b). Each module is comprised of 3 cylindrical zirconate titanate (PZT-4) elements driven at their length mode resonance frequency (Hynynen and Yin 2009, Song and Hynynen 2010). Silver electrodes were deposited on the inner and outer surfaces of the individual elements. The element dimensions, listed in table 1, were chosen to result in an equal steering range across all three driving frequencies by maintaining the elements' dimensions relative to the acoustic wavelength. Signal and ground lines were soldered to the inner and outer electrodes of each element, respectively. An exterior ring was placed around the outer-most element of each module, flush with the driving surfaces of the three elements. A thin layer of plastic film was attached to the front surface, sealing the modules and providing air loading for the cylinders.

A circuit developed in-house was used to select the desired transmit and receive frequencies for the entire array of elements for a given sonication. The receive line had a variable gain pre-amplifier to help drive the received signals along the cables. The switching circuit board was plugged into the holder and secured by 5 min epoxy (Loctite®, Henkel, Westlake, OH, USA). The signal and ground wires from the three elements were soldered to pads on the circuit board. Each complete module was connected to a controlling board. 128 modules were inserted into the hemispherical dome in a sparse arrangement that was optimized to suppress grating lobes through numerical simulations (Jones *et al* 2013). For each potential array element configuration all three frequencies of interest (see table 1) were simulated, and the chosen configuration was that which provided the best overall performance with all frequencies being weighted equally. The inserted modules were sealed using silicone rubber, and small rectangular pieces of rubber were attached to the free inner surface of the hemisphere in order to minimize acoustic reflections.

After the array construction was completed, the transducer element locations were measured using an acoustic triangulation method to account for any imperfections that may have occurred in the placement and orientation of the modules during fabrication. A narrow-band source (piezo ceramic tube; 1 mm diameter, 512 kHz center frequency) was moved to different locations in the field; at each location the source was excited with an impulse from a pulser/receiver (Panametrics, Olympus-NDT, Waltham, MA, USA) and the raw RF data were captured (612 kHz receive frequency) by a 128-channel receiver (SonixDAQ, Ultrasonix,

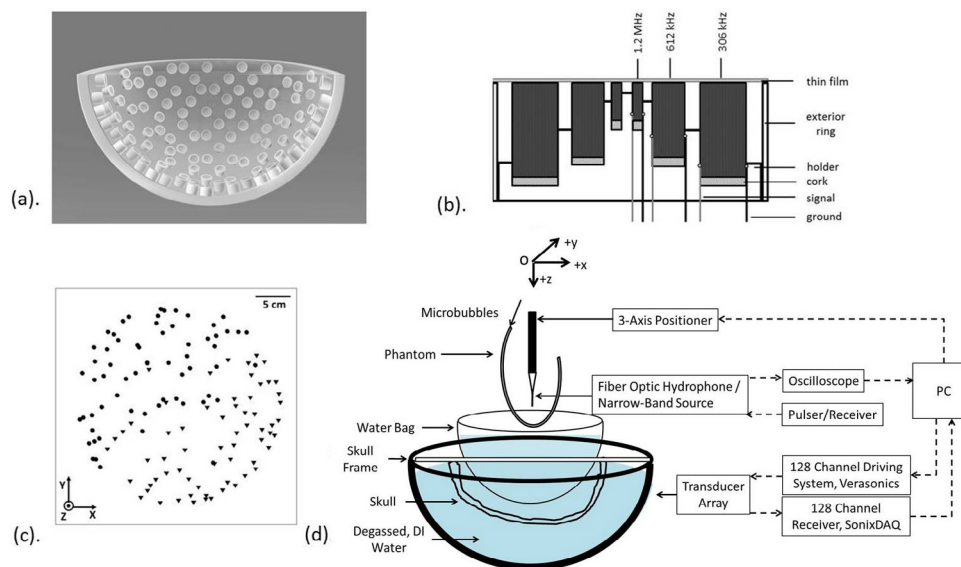


Figure 1. Cross-sectional view of (a) the fully assembled, 128-module sparse hemispherical-phased array and (b) a single module with three elements that are concentrically mounted to the holder. (c) Z-axis projection of the 612 kHz transducer array element configuration in the XY plane. The first (second) 64 elements are represented by circular (triangular) markers. (d) Experimental setup.

Table 1. Individual array element dimensions.

Driving frequency	Outer diameter (mm)	Inner diameter (mm)	Height (mm)
306 kHz	10	7	6
612 kHz	5	3.5	3
1.224 MHz	2.5	1.75	1.5

Richmond, BC, Canada) at a sampling rate of 40 MS s^{-1} . The time of flight inferred from each of the captured waveforms was used to estimate the transducer element locations (figure 1(c)) via triangulation. The central locations of the 306 kHz and 1.224 MHz elements are approximately the same as the 612 kHz elements as a result of the concentric module design.

Transmit array characterization: acoustic field measurement

The experimental setup used to characterize the array on transmit is illustrated in figure 1(d). The dome was filled with degassed/deionized water, and a water bag was used to increase the overall water level in order to minimize reflections from the water–air interface. Each of the array’s transmit frequencies was characterized separately. For single-frequency transmit characterization, the array was driven with a 5-cycle burst at a pulse repetition frequency (PRF) between 10–100 Hz by a commercially available 128-channel driving system (V-1, Verasonics, Redmond, WA, USA). A three-axis positioning system (Parker, Hannifin, PA, USA; Velmax, Broomfield, NY, USA) was centered above the dome, with a calibrated fiber optic hydrophone (Precision Acoustics, Dorset, UK) mounted parallel to the acoustical axis of the array. The speed of sound in water was estimated by recording the water temperature

(Bilaniuk and Wong 1993) using a digital thermometer (Extech Instruments, Waltham, MA, USA). The hydrophone recordings were captured on a digital oscilloscope (TDS 3012B, Tektronix, Richardson, TX, USA) and saved via General Purpose Interface Bus (GPIB) to a CPU for post-processing.

The array's focusing capabilities in water were investigated at a total of 13 target locations spanning $(-50, 50)$ mm along the X , Y , and Z axes by electronically steering the beam. At each target position, the acoustic field distribution in both the lateral and axial planes was recorded using the hydrophone for each of the array's three driving frequencies. These hydrophone measurements were repeated at the array's geometric focus while aiming within the mid-brain region of four different *ex vivo* human skullcaps (SKA, SKB, SKC, SKD as described in Jones *et al* (2015)) that were placed between the array and the focal point. The skullcaps were degassed in a vacuum jar (Nalge, Rochester, N, USA; Gast, Benton Harbor, MI, USA) at -700 mmHg for at least 2 h prior to taking measurements. Invasive source-based phase corrections (Smith *et al* 1979), obtained by analyzing the time delay between the received signals (612 kHz receive frequency) captured from the narrow-band source excited by an impulse from the pulser/receiver with and without the presence of the human skullcaps, were applied on transmit in order to compensate for the aberrations induced by the bone.

Finally, two advanced sonication strategies were tested with our system. A series of measurements were conducted where half of the array elements (circular markers in figure 1(d)) were driven at either 306 kHz or 612 kHz while the second half (triangular markers in figure 1(d)) were driven at the second-harmonic (612 kHz or 1.224 MHz, respectively), both targeting the array's geometric focus. For these measurements, the array was excited by an in-house developed driving system that enabled longer burst length excitations ($\sim 82 \mu\text{s}$, 100 Hz PRF, 1:1 amplitude ratio of the two driving frequencies), and the resulting acoustic field distributions in water were recorded. These measurements were repeated with different phase shifts (0 , $\pi/2$, and π) of the second-harmonic frequency relative to that of the fundamental driving frequency. Another set of measurements investigated the feasibility of generating a ring-shaped focal pattern near the array's geometric focus with each available driving frequency, following the optimal field generation approach outlined in Ebbini *et al* (1988) and Ibbini and Cain (1989).

Receiver array characterization: passive microbubble imaging

The receiving capabilities of the array were investigated by imaging ultrasound-stimulated microbubbles (DefinityTM, Lantheus Medical Imaging, North Billerica, MA, USA) flowing through thin-walled tube phantoms (Cole-Parmer, Vernon Hills, IL, USA). Both single-point and volumetric sonications were investigated. The microbubbles were diluted in either deionized water or saline at various dilution ratios ranging from 1:1 000 to 1:1000 000. Assuming a concentration of $(5.3 \pm 1.1) \times 10^9$ bubbles ml^{-1} for reshaken DefinityTM based on our previous measurements (O'Reilly *et al* 2014), a dilution ratio of 1:1000 000 corresponded to 5.3×10^3 bubbles ml^{-1} (0.5% of clinical dose), or approximately 1 bubble per 1 mm of tubing (tube inner diameter of 0.5 mm). The tube phantom was mounted on the three-axis positioner parallel to the array's Y -axis, as shown in figure 1(d), with its vertex placed near the array's natural focus. The microbubble solution was gravity fed through the tube phantom at a flow rate of approximately 0.43 ml min^{-1} . The transmit array was electronically focused at the vertex of the tube phantom, and the array elements of a given driving frequency excited the microbubbles with a short (5-cycle) burst at a PRF between 1–20 Hz. The resulting acoustic emissions were captured simultaneously using elements of a different frequency than those used on transmit (i.e. either the half-harmonic or second-harmonic frequency) using the previously

described 128-channel receiver with a sampling rate between 10–20 MS s⁻¹. Experiments were conducted with and without the presence of an *ex vivo* human skullcap (SKB) between the array and the tube phantom. For transcranial imaging captures, a reference sonication was also collected with either deionized water or saline only (i.e. no bubbles) flowing through the tube. Source-based skull delay corrections were collected at the geometric focus and applied on transmit to each target in the volume scans, as the skull delays were not expected to vary substantially over this relatively small scan volume (Clement and Hynynen 2002b). Table 2 summarizes the parameters employed in the various passive microbubble imaging benchtop experiments carried out in this study.

In vivo experiments

One Wistar rat (male, 307 g) was used to assess the feasibility of using the multi-frequency phased array for ultrasound-mediated FUS BBB opening and simultaneous cavitation mapping. The experimental protocol was similar to our previous studies (O'Reilly *et al* 2014, Jones *et al* 2015), and was approved by Sunnybrook Research Institute's Animal Care Committee. The rat was first anesthetized by intramuscular injecting of a mixture of ketamine (40–50 mg kg⁻¹) and xylazine (10 mg kg⁻¹). The hair on the rat's head was removed using a razor followed by the application of depilatory cream. The animal was placed supine on a platform and its head was acoustically coupled via ultrasound gel to a plastic membrane that was in contact with the water-filled array. The platform with the animal was moved between the array and a 3.0 T MRI (Magnetom Prisma, Siemens Healthcare, Erlangen, Germany) for treatment planning and BBB opening verification. *T*₂-weighted images (fast spin echo; relaxation time: 3000 ms; echo time: 82 ms; echo train length: 8; matrix size: 256 × 256; field of view: 8 × 8 cm; slice thickness: 1.5 mm) were used to select appropriate targets. The in-house developed driving system was used for this *in vivo* experiment, and the receive equipment was the same as that used for the benchtop measurements. One sonication (306 kHz driving frequency, 10 ms bursts, 1 Hz PRF, 2 min duration, 0.18 MPa estimated *in situ* pressure based on an average through rat skull transmission of 91.2% at 0.268 MHz (O'Reilly *et al* 2011)) was targeted to the mid-brain through the intact rat skull without aberration correction. A bolus of DefinityTM contrast agent (20 μl kg⁻¹) was delivered via a tail vein catheter simultaneously with the beginning of the ultrasound exposure. The received RF data were captured (10 MS s⁻¹) at the second-harmonic frequency (612 kHz), beginning with 50 μs remaining in the driving burst for a total of 800 μs, and stored for further processing. Post-treatment, gadolinium-based (100 μl kg⁻¹ Omniscan, GE Healthcare, Milwaukee, WI) contrast-enhanced *T*₁-weighted images (fast spin echo; relaxation time: 500 ms; echo time: 16 ms; echo train length: 8; matrix size: 256 × 256; field of view: 8 × 8 cm; slice thickness: 1.5 mm) were acquired to assess BBB opening.

Data processing

All data analysis was performed in MATLABTM (R2013a, Mathworks, Natick, MA, USA). For the transmit characterization experiments, at each target location the position of maximum pressure was recorded and a 2D Gaussian was fit to the lateral and axial pressure field distributions in order to extract the respective beam dimensions (i.e. full width at half maximum (FWHM)). The tilt angle of the focus, defined here as the angle between the long axis direction of the 2D fit in the axial plane and the acoustical axis (*Z*) of the dome, was also extracted.

For the passive imaging experiments, the raw RF data were post-processed and reconstructed in a similar way to that described previously (O'Reilly *et al* 2014). Briefly, the raw

Table 2. Summary of the parameters employed in the benchtop experiments for characterization of the receiver array.

Exp.	Skull insertion	Target	Tx ^a (kHz)	Rx ^a	Burst length (cyc ^a)	Bubble dilution ratio	Tube diameter size (mm)
I	No	7–13 locations	306, 612	Second-harmonic	5	1:1000000	Inner: 0.5
	Yes	Near (0, 0, 0)			5–612	1:1000–1:1000000	
II	No	7–13 locations	1224, 612	Half-harmonic	5	1:1000000	Outer: 1.1
	Yes	Near (0, 0, 0)	612		5	1:1000	
III	Yes	Volumetric scan: $2 \times 30 \times 15 \text{ mm}^3$ (step size $1 \times 0.5 \times 3 \text{ mm}^3$)	306	Second-harmonic	5	1: 1000	Inner: 0.8
		Volumetric scan: $1 \times 20 \times 14 \text{ mm}^3$ (step size $0.5 \times 0.25 \times 2 \text{ mm}^3$)	612	Half-harmonic			Outer: 1.4

^aTx: transmit frequency, Rx: receive frequency, Cyc: cycles.

RF data were filtered using a fourth-order Butterworth band-pass filter (400 kHz bandwidth centered about the receive frequency) in order to remove any DC bias as well as eliminate the transmit frequency and other noise from the signals. In the trans-skull imaging experiments, the raw RF data captured from the reference sonication (i.e. saline or deionized water only) was subtracted from the signals obtained with microbubbles present prior to filtering, in order to suppress reflections from stationary structures (e.g. skull surface, water–air interface, tubing, hydrophone) and enhance the overall contrast agent signal. The resulting filtered signals were beamformed using a variant of the ‘time exposure acoustics’ (TEA) (Norton and Won 2000) reconstruction algorithm, which was modified to include skull delay corrections (Jones *et al* 2013), over a 3D cubic reconstruction volume centered about the transmit location. The voxel size was chosen to be $\lambda/5$, where λ represents the wavelength at the receive frequency, which is a factor of 2.5 (5) smaller than lateral (axial) spatial resolution of our array (approximately $\lambda/2$ laterally and λ axially (Jones *et al* 2013, O’Reilly *et al* 2014)). For each voxel within this imaging region of interest (ROI), the signals are first scaled and delayed as follows:

$$Q_n(\mathbf{r}; t) = \hat{p}_n \left(t + \frac{\|\mathbf{r}_n - \mathbf{r}\|}{c} - s_n \right) \cdot \|\mathbf{r}_n - \mathbf{r}\|, \quad (1)$$

where $\hat{p}_n(t)$ is the filtered time-dependent pressure measured by receiver n located at \mathbf{r}_n , c is the speed of sound in water, $\|\mathbf{r}_n - \mathbf{r}\|$ notes the distance between receiver n and the voxel located at \mathbf{r} , and s_n is the skull delay correction term for receiver n . Multiplication by $\|\mathbf{r}_n - \mathbf{r}\|$ accounts for the geometric spreading that would occur during acoustic propagation from a point source located at \mathbf{r} to receiver n located at \mathbf{r}_n . An image intensity is then assigned to each voxel, $I(\mathbf{r})$, by integrating these modified signals over a time window containing microbubble activity as follows:

$$I(\mathbf{r}) = \frac{1}{T} \int_{t_0}^{t_0+T} \left[\sum_{n=1}^N \sum_{\substack{m=1 \\ n \neq m}}^N Q_n(\mathbf{r}; t) \cdot Q_m(\mathbf{r}; t) \right] dt, \quad (2)$$

where $[t_0, t_0 + T]$ defines the integration window and N is the number of elements in the array. The spectral content originating from a given voxel of interest was analyzed by examining the fast Fourier transform (FFT) of the beamformed signal at that location (i.e. $\text{FFT}\{\sum_{n=1}^N Q_n(\mathbf{r}; t)\}$). For the volumetric tube phantom scans, each frame was individually reconstructed within the same imaging ROI and normalized to its own maximum intensity. Frames containing no more than two distinct side lobes with a magnitude less than -3 dB of main lobe intensity were kept for image reconstruction, and a maximum pixel projection was taken across these frames to generate a final compound image of the tube (O’Reilly and Hynynen 2013, Jones *et al* 2015).

Results

Transmit array characterization

Figures 2(a)–(c) shows the acoustic pressure field distributions in the lateral (XY) plane generated by steering the array along the Z-axis for each of the array’s transmit frequencies. For each driving frequency, the location of maximum intensity was achieved near the array’s geometric center, and the peak pressure was found to decrease with increasing distance from the array’s geometric focus. For a fixed target location, the size of the transmit focus decreased with increasing driving frequency, owing to the reduced acoustic wavelength. The acoustic

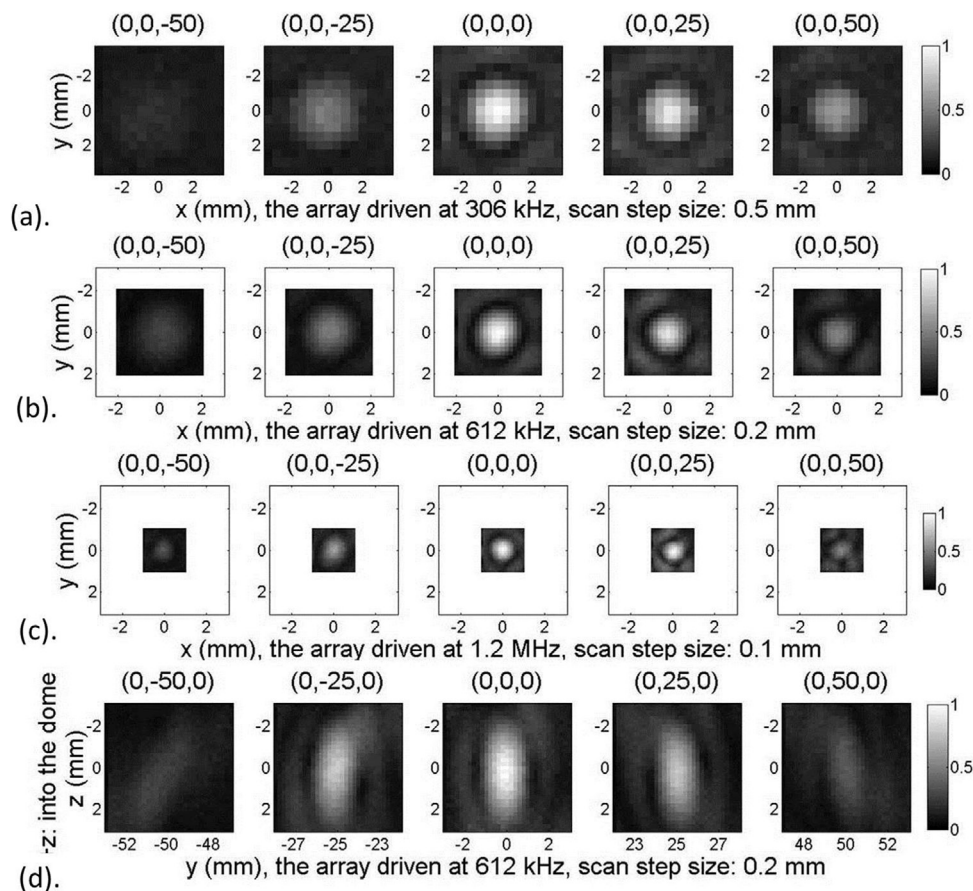


Figure 2. (a)–(c) Acoustic pressure field distributions in the XY plane for target locations of $(0, 0, 0)$, $(0, 0, \pm 25)$, and $(0, 0, \pm 50)$ mm. Results from driving the array at (a) 306 kHz, (b) 612 kHz and (c) 1.224 MHz are shown with pixel sizes of 0.5 mm, 0.2 mm, and 0.1 mm, respectively. (d) Acoustic pressure field distribution in the YZ plane for target locations of $(0, 0, 0)$, $(0, \pm 25, 0)$, and $(0, \pm 50, 0)$ mm and a driving frequency of 612 kHz (0.2 mm pixel size). In (a)–(d) each image is normalized to the peak pressure achieved at $(0, 0, 0)$ for that particular case. The peak driving voltage was held constant at 30 V, resulting in a peak focal pressure of 0.44 MPa, 0.78 MPa and 0.72 MPa at the geometric focus with a driving frequency of 306 kHz, 612 kHz and 1.224 MHz, respectively.

field distribution in the axial (YZ) plane generated by steering the array along the Y -axis at a driving frequency of 612 kHz is plotted in figure 2(d). As the beam was steered away from the array's geometric focus, the long axis of the ellipsoidal focal region became tilted with respect to the Z -axis, an effect that became more pronounced with larger steering distances (Yin and Hynynen 2005).

The systems' transmit steering capabilities for each driving frequency are quantitatively evaluated in figure 3. For each driving frequency, the peak pressure achieved decreased as the beam was steered away from the array's geometric focus in both the lateral (X/Y) and axial (Z) directions. The pressure decrease was approximately symmetric with respect to the array's geometric focus in the lateral (X/Y) directions in all cases, however, the pressure diminished

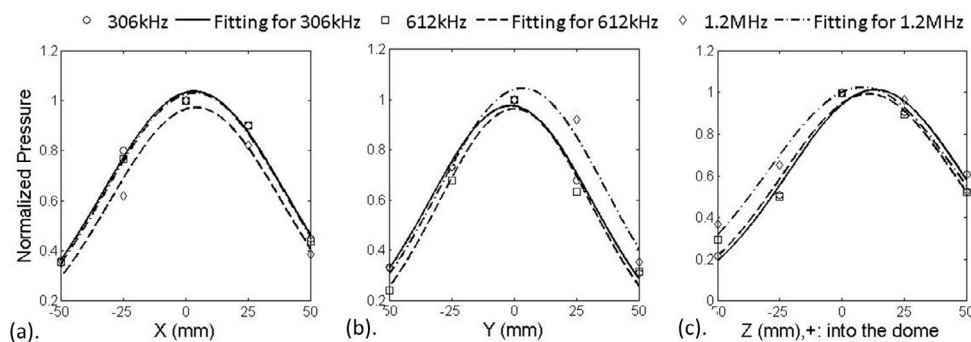


Figure 3. Maximum acoustic pressure obtained in water for different focal locations when the beam was steered along the (a) X , (b) Y , and (c) Z axes. Results from driving the array at 306 kHz (circles), 612 kHz (squares) and 1.224 MHz (triangles) are shown. The data were normalized to the maximum pressure achieved for each driving frequency. A 1D Gaussian was fit to the data at each frequency and added to the plots.

more quickly when the beam was steered out of the array ($-Z$) compared to being steered into the array ($+Z$). Table 3 summarizes the effective beam steering range for each driving frequency, which was defined as the distance from the geometric focus to the point at which the pressure drops to 50% of the peak value. Similar beam steering capabilities were achieved for each of the array's driving frequencies, covering an effective cylindrical steering volume of approximately 80 mm ($(-40, 40)$ mm) in diameter and 80 mm ($(-30, 50)$ mm) in height.

Figure 4 shows the focal spot size as a function of the target location for each of the array's transmit frequencies. In general, the pressure FWHM of the focal spot increased with decreasing transmit frequency, as expected due to the larger acoustic wavelength. Specifically, at the array's geometric center, the lateral (axial) FWHM was found to be 0.9 ± 0.1 (2.1 ± 0.1) mm, 1.7 ± 0.1 (3.9 ± 0.1) mm, and 3.1 ± 0.1 (6.5 ± 0.1) mm at 1.224 MHz, 612 kHz, and 306 kHz, respectively. For beam steering along the lateral axes, the focal volume was enlarged as the beam was steered farther away from the geometric focus. For axial beam steering, the focal volume decreased when the beam was steered into the dome ($+Z$).

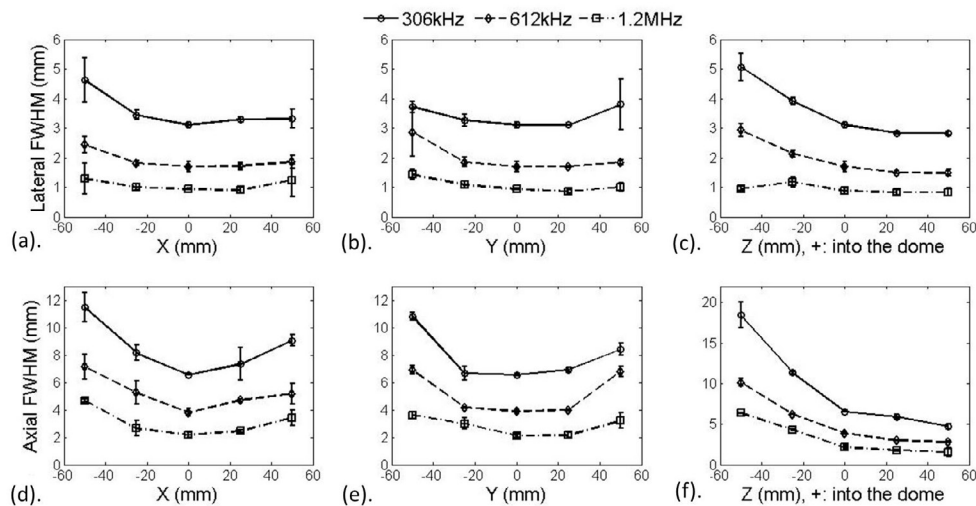
Figure 5 quantifies the change in the tilt angle as a function of the lateral steering distance from the geometric focus. It was found that the farther the beam was steered laterally, the more the focus was tilted, which agrees with the trend shown in figure 2(d), and the results of a previously simulation study (Yin and Hynynen 2005). Note that the trends are not symmetric about the zero point, due to the fact that the sparse array element layout is also aperiodic and asymmetric about this location.

Figure 6 quantifies the dependence of the targeting error, defined as the distance between the expected location of the focal target and the location of the maximum acoustic pressure, on the steering distance along each Cartesian axis for each of the array's transmit frequencies. The distances were calculated relative to the geometric focal location of each driving frequency, since the location of the natural focus was shifted out of the dome with increasing frequency: the geometric focus at 306 kHz (1.224 MHz) was found to be displaced approximately 0.2 mm into (out of) the dome relative to the location obtained at 612 kHz. The mean lateral and axial targeting errors were all below 1.0 mm over the effective steering range for each of the three transmit frequencies.

The transcranial focusing capabilities of the array at each transmit frequency are shown in figure 7, together with corresponding water-path measurements for comparison. The shape of the trans-skull focus obtained at each frequency using source-based skull corrections was

Table 3. Beam steering range along each of the Cartesian directions (*X/Y/Z*) for each of the array's driving frequencies. The errors quoted were obtained from the uncertainty in the Gaussian fitting procedure.

Transmit frequency	306 kHz	612 kHz	1.224 MHz
<i>X</i>	$\pm(45 \pm 3)$ mm	$\pm(40 \pm 4)$ mm	$\pm(44 \pm 3)$ mm
<i>Y</i>	$\pm(38 \pm 2)$ mm	$\pm(35 \pm 1)$ mm	$\pm(41 \pm 3)$ mm
<i>Z</i>	$+(55 \pm 3)$ mm $-(28 \pm 1)$ mm	$+(51 \pm 3)$ mm $-(30 \pm 2)$ mm	$+(53 \pm 3)$ mm $-(37 \pm 2)$ mm

**Figure 4.** Transmit focal size (lateral (a)–(c) and axial (d)–(f) pressure FWHM) as a function of driving frequency and target location. Results from electronic steering along the (a) and (d) *X*, (b) and (e) *Y*, and (c) and (f) *Z* axes are shown. The error bars represent one standard deviation from repeat measurements ($n = 3$).

similar to the corresponding focus measured without the presence of the human skull. The insertion of a human skullcap between the focal point and the array led to a reduction of the peak pressure measured, a shift in the focal location (on the order of 1 mm), and an increase in side lobe levels relative to the main lobe. An example of the peak acoustic pressure measured at the geometric focus with and without the insertion of a human skullcap (SKB) for each of the array's driving frequencies is given in table 4, along with the mean insertion loss calculated from measurements with the four different human skullcaps tested in this study. From table 4, it can be seen that that lower frequencies experience less attenuation when propagating through human skull bone than higher frequencies, which is consistent with previous studies (Fry 1977, Pichardo *et al* 2011).

The lateral acoustic field distributions resulting from simultaneous dual-frequency exposures are shown in figures 8(a)–(r). During dual-frequency excitation, the peak negative and peak positive pressure field distributions differ from one another, and the shape of the temporal waveforms is no longer symmetric about the null pressure line. The lateral pressure FWHM was found to be (1.4 ± 0.2) mm and (2.8 ± 0.3) mm for dual-frequency sonications at 612 kHz/1.224 MHz and 306 kHz/612 kHz, respectively. The resulting field patterns and temporal waveforms are dependent on the phase offset of the second-harmonic signals with

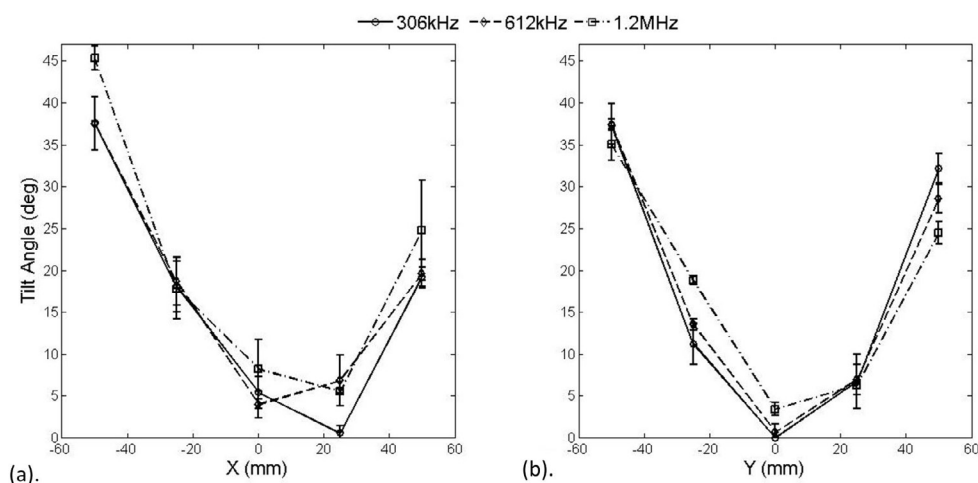


Figure 5. Dependence of the tilt angle on the steering distance away from the geometric focus in the (a) X and (b) Y directions. The error bars represent one standard deviation from multiple repeat measurements ($n = 3$).

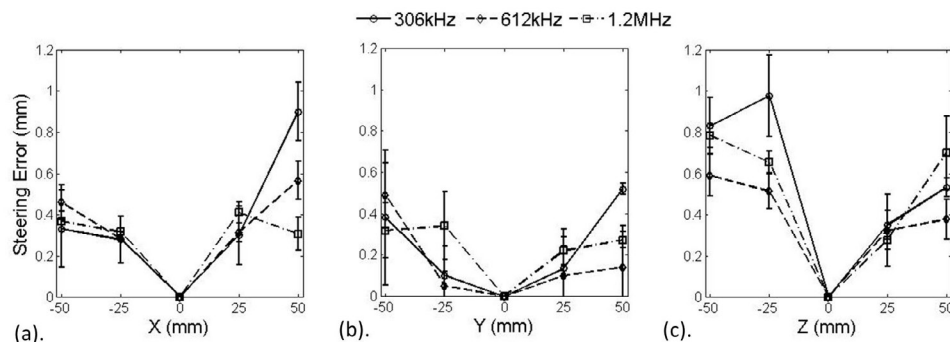


Figure 6. Targeting error as a function of the steering distance from the geometric focus in the (a) X, (b) Y, and (c) Z directions. Error bars represent one standard deviation from multiple repeat measurements ($n = 3$).

respect to that of the fundamental, and with our setup a maximum peak positive pressure was recorded for a $\pi/2$ phase offset for both of the dual-frequency cases. In figure 8(s), lateral and axial cross-sections of the ring-shaped foci generated by the phased array at each driving frequency are shown. The maximum peak negative acoustic pressure obtained in generating the ring-shaped focus at 306 kHz, 612 kHz, and 1.224 MHz has dropped 42%, 43%, and 46% of the value obtained during a single-point sonication targeted at the center of the ring using the same driving voltage, similar to the pressure drops expected from Rayleigh simulations (O'Neil 1949), which is 42%, 43%, and 42%, respectively.

Imaging array characterization

The size of the imaging point-spread function (PSF) is shown in figure 9, estimated based on measurements from dilute bubble clouds (approximately 1 bubble per 1 mm of tubing) with different transmit and receive combinations at imaging locations spanning $(-50, 50)$ mm in

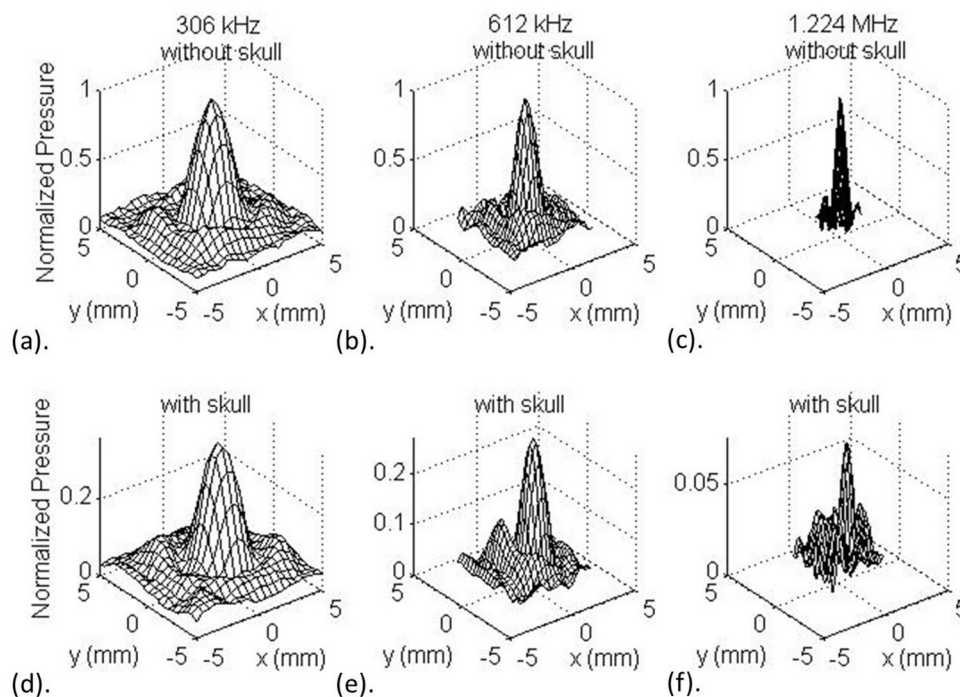


Figure 7. (a)–(f) Surface plots of the normalized acoustic pressure distribution in the *XY* plane at the array's geometric focus, by driving the array at (a) and (d) 306 kHz, (b) and (e) 612 kHz and (c) and (f) 1.224 MHz. Results from measurements taken in water (a)–(c) and with an *ex vivo* human skullcap (SKB) placed between the focal location and the array (d)–(f) are shown. The transmit array was driven with a 5-cycle burst at a PRF of 100 Hz and under a constant peak driving voltage 80 V, resulting in peak pressures of approximately 1.18 MPa, 2.09 MPa, and 1.92 MPa at 306 kHz, 612 kHz, and 1.224 MHz, respectively. The data were all normalized to the maximum pressure without the presence of the skull at each frequency.

Table 4. Acoustic pressure measured at the geometric focus by driving the array at 306 kHz, 612 kHz and 1.224 MHz at a peak voltage of 80 V with and without the presence of an *ex vivo* human skullcap (SKB). The errors of the pressure were calculated from the uncertainty of the fiber optic hydrophone system. The insertion loss was calculated by averaging the measurements from four different *ex vivo* human skullcaps, and the errors quoted represented the standard deviation.

Maximum pressure	Frequency		
	306 kHz	612 kHz	1.224 MHz
Measurements			
Without skullcap (MPa)	1.18 ± 0.15	2.09 ± 0.27	1.92 ± 0.25
With skullcap (MPa)	0.42 ± 0.05	0.57 ± 0.07	0.15 ± 0.02
Positional shift of peak pressure compared to the water case (mm)	~0.5	~0.9	~0.5
Insertion loss (%)	59 ± 7	70 ± 6	93 ± 3

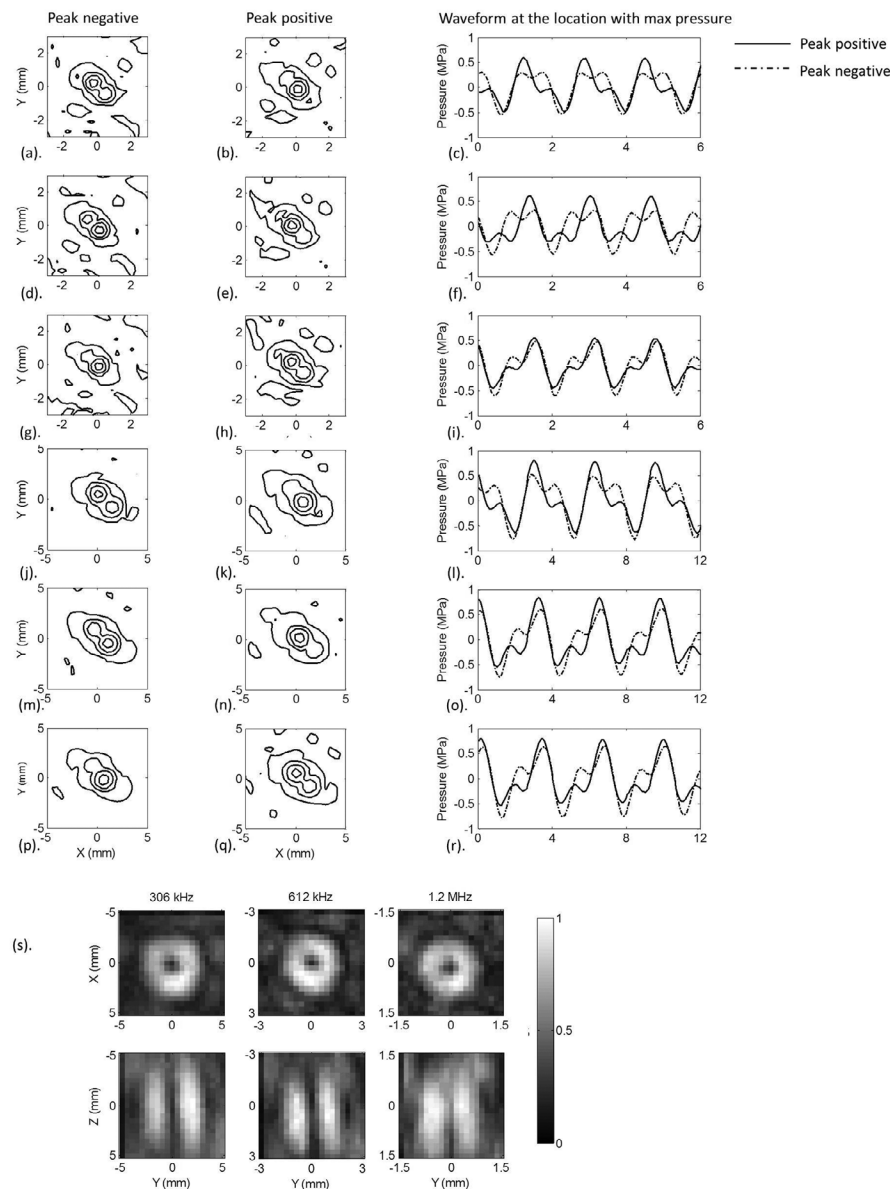


Figure 8. Lateral acoustic pressure distributions measured during dual-frequency sonications at 612kHz/1.224 MHz (a), (b), (d), (e), (g) and (h) and 306/612kHz (j), (k), (m), (n), (p) and (q) near the array's geometric center. Normalized peak negative (left column) and positive (middle column) field distributions are shown. In (a)–(r), the phase of the second-harmonic signal was shifted with respect to the fundamental as follows: (a)–(c) and (j)–(l) 0, (d)–(f) and (m)–(o) $\pi/2$, and (g)–(i) and (p)–(r) π . For each case, temporal waveforms at the point of maximum magnitude in both peak negative (dashed line) and positive (solid line) acoustic pressure are given (right column). Contours are shown every 20% from 10% to 90% on a linear scale. (s) Lateral (top row) and axial (bottom row) pressure distribution of simultaneous multi-foci sonications. At each driving frequency, a circular focus with a radius of 0.4λ was generated (5-cycle burst, 10 Hz PRF, 30 V peak driving voltage).

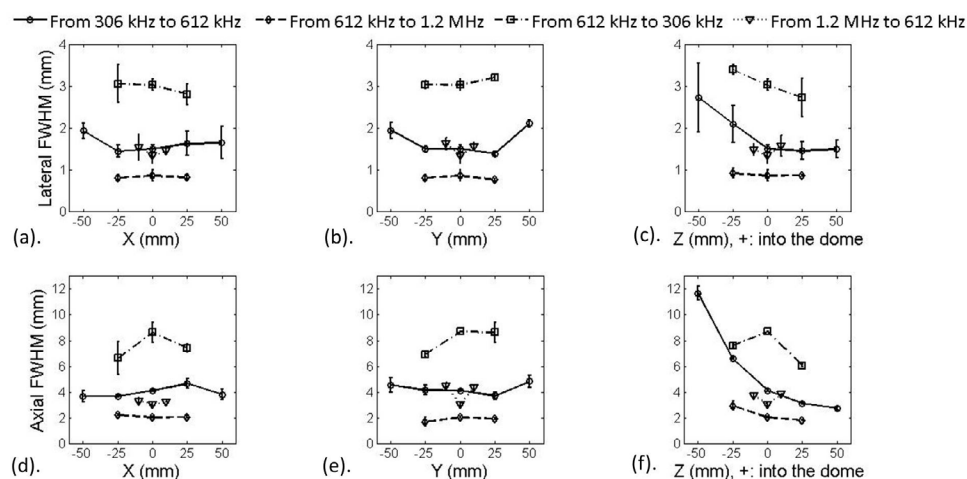


Figure 9. Intensity FWHM dimensions of the array's PSF in the (a)–(c) lateral and (d)–(f) axial directions from measurements taken in water at different locations along the (a) and (d) X-, (b) and (e) Y-, and (c) and (f) Z-directions. Error bars represent one standard deviation from multiple repeated measurements ($n = 3$). The bubble concentration was estimated to be 5.3×10^3 bubbles ml^{-1} (dilution ratio of 1:1000000).

both the lateral and axial directions. Similar trends to those found on transmit (figure 4) are observed in figure 9 based on that the PSF volume increases in size with increasing distance from the geometric focus in all directions with the exception of into the dome (+Z), which is in agreement with our previous *in silico* results (Jones *et al* 2013). A lateral (axial) intensity FWHM ranging from 0.8–3.5 mm (1.7–11.7 mm) was observed, by switching between different transmit and receive channels and imaging locations. The axial spread of the PSF was larger than the lateral direction due to a tighter focusing in the lateral plane afforded by the hemispherical element geometry. It is also expected (Norton and Won 2000) that at a fixed source location the images generated at 612 kHz would be similar for both transmit frequencies of 306 kHz (solid line with circle) and 1.224 MHz (dash line with triangle) (figure 9), while for a fixed transmit frequency of 612 kHz, the reconstructed images at 306 kHz (dash line with square) and 1.224 MHz (dash line with diamond) would be markedly different, with a smaller PSF at the higher receive frequency and vice versa (figure 9).

Figure 10(a) illustrates three examples of trans-skull microbubble cloud imaging close to the array's geometric focus both at the half-harmonic (306 kHz) of the transmit frequency (612 kHz), and at the second-harmonic with a transmit frequency of 306 kHz and 612 kHz. The use of source-based phase corrections on receive restored images with a similar focal shape and size to those obtained in the water-path case (data not shown). Additionally, the size of the main lobe decreased with increasing imaging frequency from 306 kHz to 1.224 MHz, demonstrating the potential of using second-harmonic emissions to enhance the imaging resolution during passive beamforming. In figure 10(b) the frequency spectra of the beamformed RF data at the point of maximum intensity (pointed by the arrow) for each of the three cases are given, where distinct spectral peaks at the fundamental, second harmonic, half-harmonic, and ultra-harmonic frequencies can be seen. Figure 10(c) presents compound images obtained from volumetric scans of the tube phantom through an *ex vivo* human skullcap under various combinations of transmit and receive frequencies. For the case of trans-skull imaging without

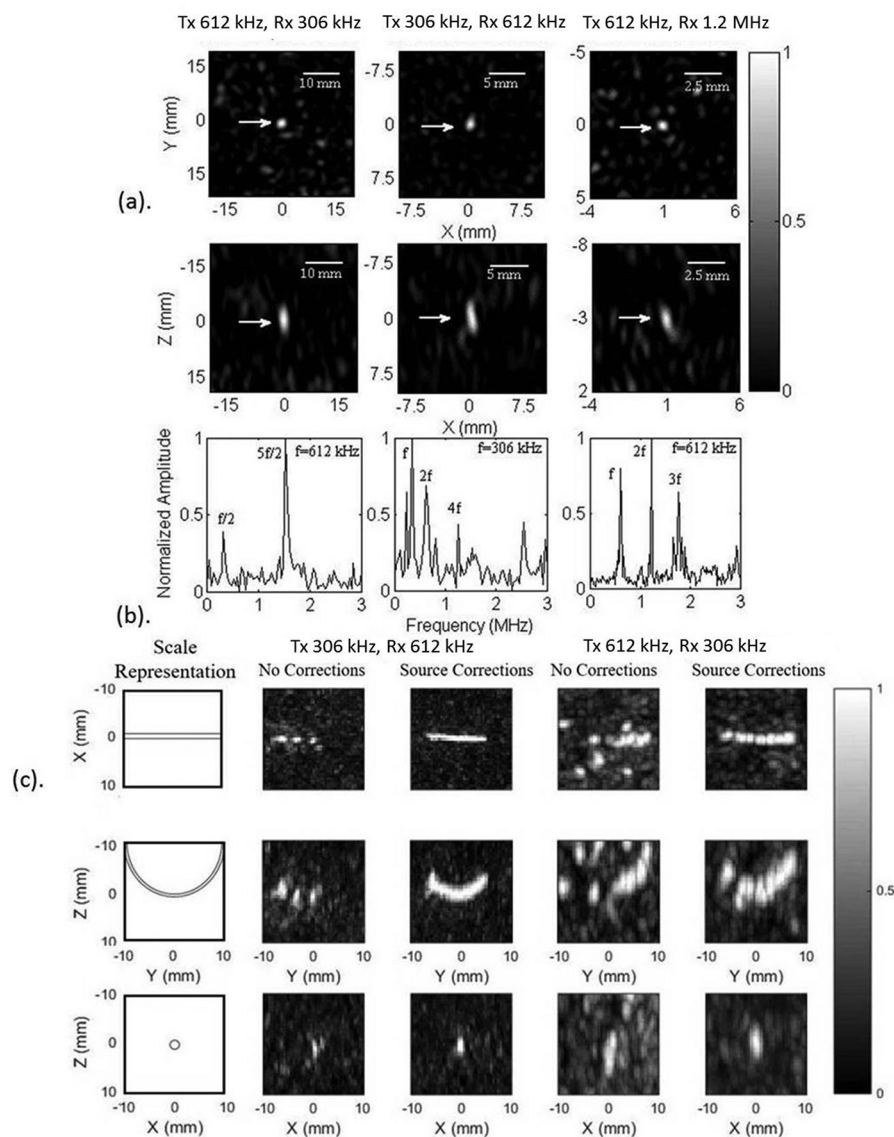


Figure 10. (a) Lateral (top row) and axial (bottom row) images of microbubble clouds located near the array's geometric focus reconstructed at 306 kHz (0.53 MPa estimated *in situ* pressure), 612 kHz (0.27 MPa estimated *in situ* pressure), and 1.224 MHz (0.23 MPa estimated *in situ* pressure), respectively, through an *ex vivo* human skullcap using source-based aberration corrections. Please note that the scale bars used in each sub plot in (a) are different. (b) Frequency spectrum of the beamformed signal at the point of maximum intensity is given for each of the cases in (a). (c) Normalized maximum pixel projection images of the tube phantom obtained through an *ex vivo* human skullcap. Images were captured at both the half-harmonic (612 kHz transmit frequency, 0.53 MPa estimated *in situ* pressure) and the second-harmonic (306 kHz transmit frequency, 0.27 MPa estimated *in situ* pressure), and were reconstructed with and without the use of source-based aberration corrections on receive. The cross-sectional images (bottom row) were generated by taking the maximum pixel projection over the range of $(-1, 1)$ mm in Y .

aberration correction on receive, the reconstructions are distorted and fail to illuminate the shape of the tube, particularly during second-harmonic imaging due to the higher source frequency. However, the inclusion of source-based skull delay corrections led to image quality improvements in both cases, resulting in a larger portion of the phantom being visible and a reduction in apparent signal originating from outside of the tube region. Sub-harmonic imaging led to higher peak side lobe ratios, as an increase in side lobe levels relative to the main lobe can be seen in the image reconstructed by the sub-harmonic signal.

Results from the *in vivo* experiment are presented in figure 11. The BBB was successfully opened in the mid-brain of the rat, as can be seen from the contrast-enhanced T_1 -weighted MR image (figure 11(a)). A spatial map of the microbubble activity at the second-harmonic frequency 30 s into the therapeutic exposures is shown in figure 11(b) and the corresponding frequency spectrum at the point with maximum intensity is displayed (figure 11(c)).

Discussion

The results of this study demonstrate the feasibility of using a multi-frequency sparse ultrasound phased array for FUS brain therapy and imaging of microbubble cavitation activity. The use of a sparse design is important for reducing the cost of the electronics and transducer construction, and it also makes phased arrays more practical at higher frequencies for applications where small focal volumes are required. Our results demonstrate that the system has the ability to perform transmit beam steering over a large volume and the potential for 3D trans-skull mapping of the bubble activity at the half- or second-harmonic with a spatial resolution that is suitable for most clinical applications. The ability to select between multiple transmit frequencies should facilitate control of the ultrasound exposures such that location-specific BBB opening can be achieved, since the *in situ* pressure amplitudes achievable with this device are sufficient at the driving frequencies employed (McDannold *et al* 2008).

Sparse arrays have been proposed in the field of ultrasonics for both active (Turnbull and Foster 1991, Davidsen and Smith 1994, Lockwood and Foster 1996) and passive (Coviello *et al* 2012, O'Reilly *et al* 2014, Jones *et al* 2015) imaging, as well as for FUS therapy (Hynynen and Jones 2016). In the current device, the transducer elements were randomly placed on a hemispherical shell in a configuration that was optimized through numerical simulations (Jones *et al* 2013), since grating lobes (on both transmit and receive) resulting from periodic, sparse arrangements can be suppressed by using an irregular layout (Goss *et al* 1996, Hutchinson *et al* 1996, Hand *et al* 2009). It is also worth noting that the hemispherical geometry naturally provides high gains near the geometric focus (Sun and Hynynen 1999), and geometrically minimizes the formation of grating lobes. As shown in figures 7(a)–(c), sharp focal spots can be achieved with our device at each of the three frequencies without the appearance of substantial grating lobes. At the geometric focus the peak side lobe level is less than 20% of the peak pressure of the main lobe, higher than the 1372-element array described by Song and Hynynen (~10% at 306 kHz near the geometric focus) (Song and Hynynen 2010), which is expected due to the smaller element count in the current system (Pajek and Hynynen 2013). A similar relationship between the peak side lobe ratio and the number of array elements also exists in the context of passive imaging (Jones *et al* 2013). Therefore, sparse arrays with higher element counts could be constructed in the future to improve upon both the transmit and receive capabilities of the present device.

The characterization of the transmit array indicates that precise, frequency dependent focal volumes can be induced in electronically controllable locations over a large effective treatment volume without the need to mechanically reposition the device. Our group's previously developed

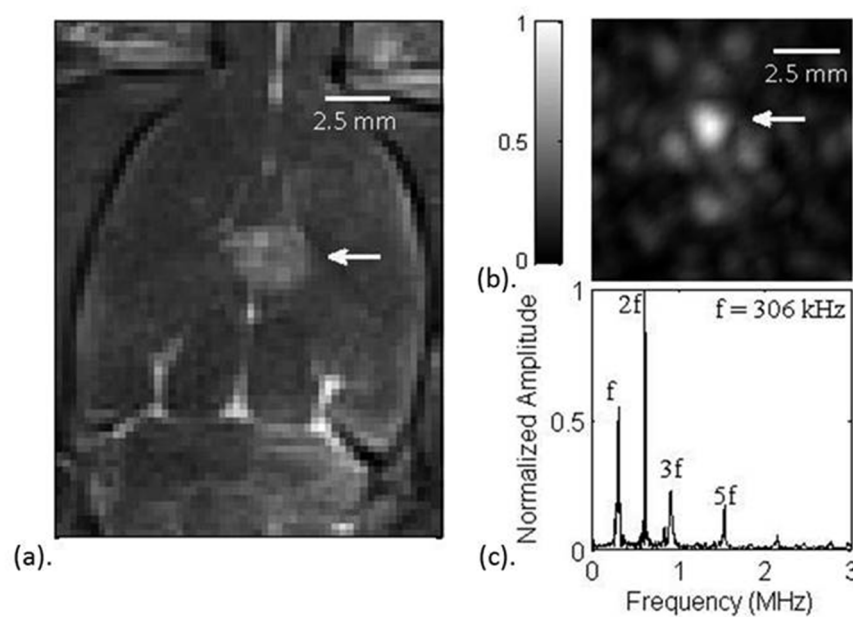


Figure 11. (a) Contrast-enhanced T_1 -weighted MR image of the rat taken with contrast following FUS + microbubbles (MBs). (b). Corresponding passive acoustic maps from the burst 30s into the sonication for sonications with MBs and BBB opening. The lateral plane of maximum intensity pixel projection is shown. (c) Frequency spectrum of the beamformed signal at the point of maximum intensity in (b) is given.

FUS brain array (Song and Hynynen 2010) was found capable of steering over cylindrical volumes of 100mm in diameter and 60mm in height (volume in which the intensity was greater than 50% of the intensity found at the geometric focus). In terms of the 50% intensity drop-off point, the present array is capable of steering over cylindrical volumes of approximately 62mm in diameter and 56mm in height at 306kHz, smaller than the steering range of the 1372-element prototype (Song and Hynynen 2010) at the same frequency, though this was anticipated due to the reduced element count (Pajek and Hynynen 2013). However, since the size of the individual elements relative to the acoustic wavelength was maintained across all three operating frequencies (table 1), the steering range at higher frequencies has been substantially improved (figure 2) with this device compared to the aforementioned array (Song and Hynynen 2010).

Compared to the relatively symmetric pressure distribution along the lateral axes, the pressure diminished more quickly when the beam was steered out of the array ($-Z$) compared to the case of steering into the array ($+Z$). This asymmetry along the Z axis is also shown in figures 4(c) and (f), as the focal volume decreases when the beam is steered into the dome, resulting from an increase in the effective array aperture. The ratio between the axial and lateral pressure FWHM near the geometric focus is close to the expected value of 2 for a hemispherical aperture. The strong steering capabilities of our system combined with the different focal sizes provided by the ability to select from multiple transmit frequencies could be beneficial in future *in vivo* experiments. For example, if the target area is larger than 3 mm in diameter and is located close to the geometric center, the frequency of 306kHz (lateral FWHM: ~ 3 mm at (0, 0, 0)) could be selected. On the other hand, if the target is located close to the skull bone and away from the array's geometric center, higher frequencies might be more favorable, as the increase in focal volume with increasing steering distance needs to be taken into account.

At the highest frequency (1.224 MHz) the pressure amplitude achieved through the skull may not be sufficient for ultrasound-mediated BBB opening at large steering distances, due to limitations with our current driving system. In the future, higher input voltages could be used to increase the *in situ* pressure. On the other hand, arrays with higher element counts could be constructed to overcome the attenuation losses at higher (>1 MHz) frequencies (Clement *et al* 2000, Pajek and Hynynen 2013).

The acoustic field distributions of dual-frequency excitation near the geometric center were measured (figures 8(a)–(r)), demonstrating the capability of using our multi-frequency transducer array for studies exploring more complex excitation fields (Lin *et al* 2014, Liu *et al* 2014, Sasaki *et al* 2014). The shape of the pressure waveform (figures 8(c), (f), (i), (l), (o) and (r)) at the focus varied depending on the phase offset of the two driving frequencies, which is consistent with the results of a previous study (Sasaki *et al* 2014), and results in a difference between the peak positive and peak negative acoustic field distributions. The maximum peak positive pressure was achieved for a relative phase offset of $\pi/2$ in both dual-frequency excitation cases (figures 8(d)–(f) and (m)–(o)), which was expected since the fundamental and second harmonic signals constructively interfered at the positive peak and destructively interfered at the negative peak. To achieve a maximal peak negative pressure, a relative phase shift of $(3/2)\pi$ could be employed. In the future, the microbubble emissions arising from dual-frequency sonications will be investigated through both benchtop and animal experiments, as it has been suggested that dual-frequency excitation can enhance cavitation activity (Liu and Hsieh 2009, Zhang *et al* 2009) and has the potential to enhance FUS-BBB opening (Liu *et al* 2014).

A second complex sonication strategy demonstrated in this study is to simultaneously generate ring-shaped focuses with variable diameter (figure 8(s)). The even pressure distribution on the ring can be further improved by scaling the pressure amplitude according to the transmit signal strength on each element, which will be tested in the future. Multi-focus sonication strategies have mainly been investigated in the context of hyperthermia (Ebbini *et al* 1988, Ibbini and Cain 1989, McGough *et al* 1992, Partanen *et al* 2013) and thermal ablation (Fan and Hynynen 1995, Wan *et al* 1996). Under the same transmit conditions, this ring focus generated a reduced peak negative pressure as expected. Besides, the treatment area is increased within the same amount of sonication time, which may be beneficial to large volume treatment. Thirdly, the use of multi-foci sonication is able to minimize energy deposition at the required locations by generating pressure field minima, e.g. the center of the ring, defined as anti-foci (Seo and Lee 2009), which may be useful in specific FUS brain therapy (Pulkkinen *et al* 2011). In short, using this phased array with multiple frequency channels, more complex sonication/receive strategies can be studied, to develop better treatment and monitoring strategies.

The receiver array allowed for the generation of spatial maps of the bubble emissions at both the half- and second-harmonic of the driving frequency during ultrasonic excitation. Imaging of dilute bubble clouds in the ultrasound field without the *ex vivo* human skullcap allowed for the PSF of the receiver arrays to be estimated at various locations within the field (figure 9). Similar to the case on transmit, the size of the PSF decreased for microbubbles placed into the dome in the (+Z) axial direction relative to the geometric focus, while it increased at locations away from the geometric focus in the lateral direction (figure 9), which is consistent with our previous numerical work (Jones *et al* 2013). These results also confirm that the size of the imaging PSF from dilute bubble clouds is primarily determined by the receiving frequency during passive beamforming (Jones *et al* 2013), since the microbubbles employed in this study (DefinityTM; 1–3 μm mean diam.) are much smaller than the size of our transmit focus.

The transcranial transmit/receive capabilities of the multi-frequency hemispherical array were assessed. In this study, our device is capable of detecting diluted microbubble (around 1 bubble per 1 mm of tubing) emissions through an intact human skullcap when driving at the lowest frequency (306 kHz) and imaging at the second harmonic (612 kHz) (figure 10(a) middle column). Our results were comparable to our work using a previous generation of array (O'Reilly *et al* 2014, Jones *et al* 2015). Microbubble signal (~1 bubble per 1 mm of tubing) was detected approximately every 13 frames (~600 ms at the PRF of 20 Hz), resulting in two good frames out of 16 frames per capture. The passive acoustic mapping from single point sonication didn't show the elongation of the main lobe in the XY plane although the tube had an elongated shape along Y-axis. This is because the peak negative voltage at the focus was at the threshold to induce microbubble stable oscillation, and the pressure would drop below the threshold value in the other region of the focus resulting in the failure to image more microbubbles and the non-elongated shape. Trans-skull mapping of microbubble activity at the sub-harmonic frequency was also demonstrated (figures 10(a) and (c)), which shows the feasibility of implementing a sub-harmonic-based feedback controller (O'Reilly and Hynynen 2012) into the array and the great potential to enhance the contrast-to-tissue ratio in PAM. Being able to observe both the second harmonic and sub-harmonic provides greater flexibility for the development of treatment control techniques since these two frequency bands indicate different regimes of bubble activity.

There are more side lobes in the images received 306 kHz and 1.224 MHz than the rest (figure 10(a)), which is because the bubble concentration was much larger in those cases. Besides, one side lobe with intensity higher than 50% of the maximum was shown near the target in the second harmonic image at 1.224 MHz (figure 10(a) right column), which was also due to the increased attenuation coefficient for higher frequencies in skull (Fry and Barger 1978). It is well known that in the presence of the skull bone leads to increased side lobe levels during passive imaging with TEA, compared to water-path controls, even when appropriate skull aberrations are included in the image reconstruction process (Jones *et al* 2013, Jones *et al* 2015, Jones and Hynynen 2016). More sophisticated beamforming algorithms, previously developed in other fields of study, have recently been applied to map acoustic activity during the application of FUS, in order to improve the resulting image quality. For example, one study employed sparse-aperture weighted beamforming (Kozick and Kassam 1991) with a 2D boundary array (2.4 cm × 2.4 cm aperture) (Coviello *et al* 2012) and demonstrated a marginal improvement (22% decrease laterally, 25% decrease axially) in the resulting size of the free-field PSF compared to that found using TEA. Another study by the same group employed robust capon beamforming (Stoica *et al* 2003) with a 1D linear array (3.8 cm aperture) (Coviello *et al* 2015) and demonstrated a reduction in the presence of tail artifacts that can occur using TEA with small-aperture arrays when bubble clouds are present within the transmit volume (Coviello *et al* 2013). However, these tail artifacts have not been observed when large-aperture receiver arrays are employed, either in simulations (Jones *et al* 2013) or experiments (O'Reilly *et al* 2014, Jones *et al* 2015, Jones and Hynynen 2016). Nevertheless, the application of more advanced reconstruction algorithms for improved image quality is warranted, and will be the subject of further investigation.

Strong signal peaks at the sub- and ultra-harmonics were detected in the frequency domain (figure 10(b)), which demonstrates the ability of using our system to monitor bubble cavitation activity with less interference from skull/tissue reflections, since sub- and ultra-harmonic signals are only generated from bubble oscillations (Shankar *et al* 1998, Biagi *et al* 2007), as opposed to harmonic signals which can also arise from nonlinear propagation in tissue (Bacon 1984, Starritt *et al* 1985, Humphrey 2000).

In the tube phantom volume scans, a larger portion of the tube became visible after source-based skull delay corrections were applied. The ends of the tube were not revealed in figure 10(c), which was probably due to the dropped acoustic pressure below the microbubble stable cavitation threshold at a further steering depth and can be improved by increasing the acoustic output power. The PAM of the phantom volumetric scan demonstrates the potential of adapting our control algorithm (O'Reilly and Hynynen 2012) to include the spatial information obtained from passive imaging, allowing for further control and optimization of the transmit sonication patterns. Furthermore, it shows the potential of non-invasively imaging microvessels in the brain by using the array, since non-invasive CT-based skull bone aberration correction is able to achieve similar correcting effects as the invasive source-based method, as demonstrated in our previous work (Jones *et al* 2015).

Finally, results from the *in vivo* experiment demonstrated the system's capability to induce ultrasound-mediated blood–brain barrier opening and simultaneously form spatial maps of microbubble cavitation activity in a rat model. The location of the maximum intensity in the reconstructed image (figure 11(b)) mapping the microbubble cavitation was close to the position where BBB opening occurred on the T_1 -weighted MR image (figure 11(a)) after coordinate system registration of the phased array to the MR. The side lobe shown on the reconstructed image (figure 11(b)) was probably due to the presence of the rat's skull and the lack of phase-correction on both transmit and receive. The preliminary *in vivo* experimental results demonstrate the potential of using the system in microbubble-mediated transcranial therapy monitoring, which requires the implementation of a real-time feed-back controller (O'Reilly and Hynynen 2012) into the driving system in the future.

Conclusion

A three-frequency, sparse hemispherical phased array was designed and characterized for microbubble-mediated FUS brain treatments. Our results indicate that the device has a clinically-relevant steering range at each of the available transmit frequencies, and can allow for frequency-controlled treatment volume size. The availability of multiple frequencies also enabled dual-frequency acoustic excitation, which will serve as a useful platform for investigating the effects of dual-frequency exposures on both microbubble cavitation activity and BBB opening efficiency. The use of the array on receive enabled spatial mapping of microbubble activity through an intact human skullcap at both the second-harmonic and half-harmonic frequencies, allowing different types of bubble activity to be analyzed. Preliminary *in vivo* experiments demonstrated the ability of the system to spatially map microbubble activity in a rat model during FUS-mediated BBB opening. Future work will focus on using the array to perform actively controlled BBB opening experiments *in vivo*.

Acknowledgments

The authors would like to thank Fedon Orfanidis, Yin Yang, Tyler Portelli, Kogee Leung, and Nathan Lim for their technical assistance. This work was supported by the National Institutes of Health under Grant No. EB003268 and EB00903, the Canada Research Chairs Program, and a grant from Weston Brain Institute. RMJ was supported by a Natural Sciences and Engineering Research Council of Canada Alexander Graham Bell Canada Graduate Scholarship.

References

- Alexandrov A V *et al* 2004 Ultrasound-enhanced systemic thrombolysis for acute ischemic stroke *New Engl. J. Med.* **351** 2170–8
- Arvanitis C D, Livingstone M S and McDannold N 2013 Combined ultrasound and MR imaging to guide focused ultrasound therapies in the brain *Phys. Med. Biol.* **58** 4749–61
- Arvanitis C D, Livingstone M S, Vykhodtseva N and McDannold N 2012 Controlled ultrasound-induced blood–brain barrier disruption using passive acoustic emissions monitoring *PLoS One* **7** e45783
- Aryal M *et al* 2013 Multiple treatments with liposomal doxorubicin and ultrasound-induced disruption of blood–tumor and blood–brain barriers improve outcomes in a rat glioma model *J. Control. Release* **169** 103–11
- Aubry J F *et al* 2003 Experimental demonstration of noninvasive transskull adaptive focusing based on prior computed tomography scans *J. Acoust. Soc. Am.* **113** 84–93
- Bacon D R 1984 Finite amplitude distortion of the pulsed fields used in diagnostic ultrasound *Ultrasound Med. Biol.* **10** 189–95
- Biagi E, Breschi L, Vannacci E and Masotti L 2007 Stable and transient subharmonic emissions from isolated contrast agent microbubbles *IEEE Trans. Ultrason. Ferroelect. Freq. Control* **54** 480–97
- Bilaniuk N and Wong G S K 1993 Speed of sound in pure water as a function of temperature *J. Acoust. Soc. Am.* **93** 1609–12
- Burgess A *et al* 2012 High-intensity focused ultrasound (HIFU) for dissolution of clots in a rabbit model of embolic stroke *PLoS One* **7** e42311
- Burns P N *et al* 1994 Harmonic power mode Doppler using microbubble contrast agents: an improved method for small vessel flow imaging *Proc. IEEE Ultrasonics Symp.* **3** 1547–50
- Chang W S *et al* 2014 Unilateral magnetic resonance guided focused ultrasound thalamotomy for essential tremor: practices and clinicoradiological outcomes *J. Neurol. Neurosurg. Psychiatry* **86** 257–64
- Chi O Z, Wei H M, Lu X and Weiss H R 1996 Increased blood–brain permeability with hyperosmolar mannitol increases cerebral O₂ consumption and O₂ supply/consumption heterogeneity *J. Cereb. Blood Flow Metab.* **16** 327–33
- Choi J, Pernot M, Small S and Konofagou E 2007 Noninvasive, transcranial and localized opening of the blood–brain barrier using focused ultrasound in mice *Ultrasound Med. Biol.* **33** 95–104
- Clement G T and Hynynen K 2002a A non-invasive method for focusing ultrasound through the human skull *Phys. Med. Biol.* **47** 1219–36
- Clement G T and Hynynen K 2002b Micro-receiver guided transcranial beam steering *IEEE Trans. Ultrason. Ferroelect. Freq. Control* **49** 447–53
- Clement G T, Sun J, Giesecke T and Hynynen K 2000a A hemisphere array for non-invasive ultrasound brain therapy and surgery *Phys. Med. Biol.* **45** 3707–19
- Clement G T, White J P and Hynynen K 2000b Investigation of a large area phased array for focused ultrasound surgery through the skull *Phys. Med. Biol.* **45** 1071–83
- Coluccia D *et al* 2014 First noninvasive thermal ablation of a brain tumor with MR-guided focused ultrasound *J. Ther. Ultrasound* **2** 1–7
- Coviello C *et al* 2012 Thin-film sparse boundary array design for passive acoustic mapping during ultrasound therapy *IEEE Trans. Ultrason. Ferroelect. Freq. Control* **59** 2322–30
- Coviello C *et al* 2013 Passive acoustic mapping using optimal beamforming for real-time monitoring of ultrasound therapy *Proc. Mtgs Acoust.* **19** 075024
- Coviello C *et al* 2015 Passive acoustic mapping utilizing optimal beamforming in ultrasound therapy monitoring *J. Acoust. Soc. Am.* **137** 2573–85
- Daidsen R E, Jensen J A and Smith S W 1994 Two-dimensional random arrays for real time volumetric imaging *Ultrason. Imaging* **16** 143–63
- Ebbini E S, Ibbini M S and Cain C A 1988 An inverse method for hyperthermia phased-array pattern synthesis *Proc. IEEE Ultrasonics Symp.* pp 947–50
- Elias W J *et al* 2013 A pilot study of focused ultrasound thalamotomy for essential tremor *New Engl. J. Med.* **369** 640–8
- Fan X and Hynynen K 1995 Control of the necrosed tissue volume during noninvasive ultrasound surgery using a 16-element phased array *Med. Phys.* **22** 297–306
- Fry F J 1977 Transskull transmission of an intense focused ultrasonic beam *Ultrasound Med. Biol.* **3** 179–84
- Fry F J and Barger J E 1978 Acoustical properties of the human skull *J. Acoust. Soc. Am.* **63** 1576–90

- Fry W J and Fry F J 1960 Fundamental neurological research and human neurosurgery using intense ultrasound *IRE Trans. Med. Electron.* **ME-7** 166–81
- Gâteau J et al 2010 Transcranial ultrasonic therapy based on time reversal of acoustically induced cavitation bubble signature *IEEE Trans. Biomed. Eng.* **57** 134–44
- Goss S A et al 1996 Sparse random ultrasound array for focal surgery *IEEE Trans. Ultrason. Ferroelect. Freq. Control* **43** 1111–21
- Gyongy M and Coussios C-C 2010 Passive spatial mapping of inertial cavitation during hifu exposure *IEEE Trans. Biomed. Eng.* **57** 48–56
- Hand J W et al 2009 A random phased array device for delivery of high intensity focused ultrasound *Phys. Med. Biol.* **54** 5675–93
- Hindman J C 1966 Proton resonance shift of water in gas and liquid states *J. Chem. Phys.* **44** 4582–92
- Humphrey V F 2000 Nonlinear propagation in ultrasonic fields: measurements, modelling and harmonic imaging *Ultrasonics* **38** 267–72
- Hutchinson E B, Buchanan M T and Hynynen K 1996 Design and optimization of an aperiodic ultrasound phased array for intracavitary prostate thermal therapies *Med. Phys.* **23** 767–76
- Hynynen K et al 2004 500-element ultrasound phased array system for noninvasive focal surgery of the brain: a preliminary rabbit study with *ex vivo* human skulls *Magn. Reson. Med.* **52** 100–7
- Hynynen K and Jolesz F A 1998 Demonstration of potential non-invasive ultrasound brain therapy through an intact skull *Ultrasound Med. Biol.* **24** 275–83
- Hynynen K and Jones R 2016 Image-guided ultrasound phased arrays are a disruptive technology for non-invasive therapy *Phys. Med. Biol.* **61** R206–48
- Hynynen K, McDannold N, Clement G T and Jolesz F A 2006 Pre-clinical testing of a phased array ultrasound system for MRI-guided noninvasive surgery of the brain—a primate study *Eur. J. Radiol.* **59** 149–56
- Hynynen K, McDannold N, Vykhodtseva N and Jolesz F A 2001 Noninvasive MR imaging-guided focal opening of the blood–brain barrier in rabbits *Radiology* **220** 640–6
- Hynynen K and Yin J 2009 Lateral mode coupling to reduce the electrical impedance of small elements required for high power ultrasound therapy phased arrays *IEEE Trans. Ultrason. Ferroelect. Freq. Control* **56** 557–64
- Ibbini M S and Cain C A 1989 A field conjugation method for direct synthesis of hyperthermia phased-array heating patterns *IEEE Trans. Ultrason. Ferroelect. Freq. Control* **36** 3–9
- Jeanmonod E et al 2012 Transcranial magnetic resonance imaging-guided focused ultrasound: noninvasive central lateral thalamotomy for chronic neuropathic pain *Neurosurg. Focus* **32** 1–11
- Jones R M and Hynynen K 2016 Comparison of analytical and numerical approaches for CT-based aberration correction in transcranial passive acoustic imaging *Phys. Med. Biol.* **61** 23–36
- Jones R M, O'Reilly M A and Hynynen K 2013 Transcranial passive acoustic mapping with hemispherical sparse arrays using CT-based skull-specific aberration corrections: a simulation study *Phys. Med. Biol.* **58** 4981–5005
- Jones R M, O'Reilly M A and Hynynen K 2015 Experimental demonstration of passive acoustic imaging in the human skull cavity using CT-based aberration corrections *Med. Phys.* **42** 4385–400
- Kinoshita M, McDannold N, Jolesz F A and Hynynen K 2006 Noninvasive localized delivery of Herceptin to the mouse brain by MRI-guided focused ultrasound-induced blood–brain barrier disruption *Proc. Natl Acad. Sci. USA* **103** 11719–23
- Kozick R J and Kassam S A 1991 Linear imaging with sensor arrays on convex polygonal boundaries *IEEE Trans. Syst. Man Cybern.* **21** 1155–66
- Lapchak P A and Araujo D M 2007 Advances in hemorrhagic stroke therapy: conventional and novel approaches *Expert Opin. Emerg. Drugs* **12** 389–406
- Lin K W et al 2014 Synthesis of monopolar ultrasound pulses for therapy: the frequency-compounding transducer *IEEE Trans. Ultrason. Ferroelect. Freq. Control* **61** 1123–36
- Lipsman N et al 2013 MR-guided focused ultrasound thalamotomy for essential tremor: a proof-of-concept study *Lancet Neurol.* **12** 462–8
- Liu H L, Chen H W, Kuo Z H and Huang W C 2008 Design and experimental evaluations of a low-frequency hemispherical ultrasound phased-array system for transcranial blood–brain barrier disruption *IEEE Trans. Biomed. Eng.* **55** 2407–16
- Liu H-L et al 2010 Blood–brain barrier disruption with focused ultrasound enhances delivery of chemotherapeutic drugs for glioblastoma treatment *Radiology* **255** 415–25
- Liu H-L et al 2014 Design and experimental evaluation of a 256-channel dual-frequency ultrasound phased-array system for transcranial blood–brain barrier opening and brain drug delivery *IEEE Trans. Biomed. Eng.* **61** 1350–60

- Liu H L and Hsieh C M 2009 Single-transducer dual-frequency ultrasound generation to enhance acoustic cavitation *Ultrason. Sonochem.* **16** 431–8
- Lockwood G R and Foster F S 1996 Optimizing the radiation pattern of sparse periodic two-dimensional arrays *IEEE Trans Ultrason. Ferroelect. Freq. Control* **43** 15–9
- Magara A et al 2014 First experience with MR-guided focused ultrasound in the treatment of Parkinson's disease *J. Ther. Ultrasound* **2** 11
- Marquet F et al 2013 Non-invasive ultrasonic surgery of the brain in non-human primates *J. Acoust. Soc. Am.* **134** 1632–9
- Martin E et al 2009 High-intensity focused ultrasound for noninvasive functional neurosurgery *Ann. Neurol.* **66** 858–61
- Matsunaga S et al 2010 Gamma knife surgery for metastatic brain tumors from primary breast cancer: treatment indication based on number of tumors and breast cancer phenotype *J. Neurosurg.* **113** 65–72
- McDannold N 2005 Quantitative MRI-based temperature mapping based on the proton resonant frequency shift: review of validation studies *Int. J. Hyperthermia* **21** 533–46
- McDannold N et al 2010 Transcranial magnetic resonance imaging-guided focused ultrasound surgery of brain tumors: initial findings in 3 patients *Neurosurgery* **66** 323–32
- McDannold N, Vykhodtseva N and Hynynen K 2006 Targeted disruption of the blood–brain barrier with focused ultrasound: association with cavitation activity *Phys. Med. Biol.* **51** 793–807
- McDannold N, Vykhodtseva N and Hynynen K 2008 Blood-brain barrier disruption induced by focused ultrasound and circulating preformed microbubbles appears to be characterized by the mechanical index *Ultrasound Med. Biol.* **34** 834–40
- McGough R J, Ebbini E S and Cain C 1992 A direct computation of ultrasound phased-array driving signals from a specified temperature distribution for hyperthermia *IEEE Trans. Biomed. Eng.* **39** 825–35
- Mulvagh S L et al 1996 Second harmonic imaging of an intravenously administered echocardiographic contrast agent: visualization of coronary arteries and measurement of coronary blood flow *J. Am. Coll. Cardiol.* **27** 1519–25
- Nau R, Sorgel F and Eiffert H 2010 Penetration of drugs through the blood-cerebrospinal fluid/blood–brain barrier for treatment of central nervous system infections *Clin. Microbiol. Rev.* **23** 858–83
- Norton S J and Won I J 2000 Time exposure acoustics *IEEE Trans. Geosci. Remote Sens.* **38** 1337–43
- O'Neil H T 1949 Theory of focusing radiators *J. Acoust. Soc. Am.* **21** 516–26
- O'Reilly M A, Jones R M and Hynynen K 2014 3D transcranial ultrasound imaging of microbubble clouds using a sparse hemispherical array *IEEE Trans. Biomed. Eng.* **61** 1285–94
- O'Reilly M A and Hynynen K 2012 Blood–brain barrier: real-time feedback-controlled focused ultrasound disruption by using an acoustic emissions-based controller *Radiology* **263** 96–106
- O'Reilly M A and Hynynen K 2013 A super-resolution ultrasound method for brain vascular mapping *Med. Phys.* **40** 110701
- O'Reilly M A, Muller A and Hynynen K 2011 Ultrasound insertion loss of rat parietal bone appears to be proportional to animal mass at sub-megahertz frequencies *Ultrasound Med. Biol.* **37** 1930–7
- Pajek D and Hynynen K 2013 The application of sparse arrays in high frequency transcranial focused ultrasound therapy: a simulation study *Med. Phys.* **40** 122901
- Partanen A et al 2013 Reduction of peak acoustic pressure and shaping of heated region by use of multifoci sonications in MR-guided high-intensity focused ultrasound mediated mild hyperthermia *Med. Phys.* **40** 013301
- Pasovic M et al 2011 Second harmonic inversion for ultrasound contrast harmonic imaging *Phys. Med. Biol.* **56** 3163–80
- Pernot M et al 2007 *In vivo* transcranial brain surgery with an ultrasonic time reversal mirror *J. Neurosurg.* **106** 1061–6
- Pichardo S, Sin V W and Hynynen K 2011 Multi-frequency characterization of the speed of sound and attenuation coefficient for longitudinal transmission of freshly excised human skulls *Phys. Med. Biol.* **56** 219–50
- Pulkkinen A, Huang Y, Song J and Hynynen K 2011 Simulations and measurements of transcranial low-frequency ultrasound therapy: skull-base heating and effective area of treatment *Phys. Med. Biol.* **56** 4661–68
- Riordan M and Tovar-Spinoza Z 2014 Laser induced thermal therapy (LITT) for pediatric brain tumors: case-based review *Transl. Pediatr.* **3** 229–35

- Salgaonkar V A, Datta S, Holland C K and Mast T D 2009 Passive cavitation imaging with ultrasound arrays *J. Acoust. Soc. Am.* **126** 3071–83
- Sasaki H *et al* 2014 Highly efficient cavitation-enhanced heating with dual-frequency ultrasound exposure in high-intensity focused ultrasound treatment *Japan. J. Appl. Phys.* **53** 07KF11
- Seo J and Lee J 2009 Anti-foci for focused ultrasound *Int. J. Hyperthermia* **25** 566–80
- Shankar P M, Dala Krishna P and Newhouse V L 1998 Advantages of subharmonic over second harmonic backscatter for contrast-to-tissue echo enhancement *Ultrasound Med. Biol.* **24** 395–9
- Smith S W, Phillips D J, von Ramm O T and Thurstone F L 1979 Some advances in acoustic imaging through skull *Ultrasonic Tissue Characterization II (National Bureau of Standards, Special Publication 525)* ed M Linzer (Washington, DC: US Government Printing Office) pp 209–18
- Sokka S D, Gauthier T P and Hynynen K 2005 Theoretical and experimental validation of a dual-frequency excitation method for spatial control of cavitation *Phys. Med. Biol.* **50** 2167–79
- Song J and Hynynen K 2010 Feasibility of using lateral mode coupling method for a large scale ultrasound phased array for noninvasive transcranial therapy *IEEE Trans. Biomed. Eng.* **57** 124–33
- Starratt H C, Perkins M A, Duck F A and Humphrey V F 1985 Evidence for ultrasonic finite-amplitude distortion in muscle using medical equipment *J. Acoust. Soc. Am.* **77** 302–6
- Stoica P, Wang Z and Li J 2003 Robust capon beamforming *IEEE Signal Proc. Lett.* **10** 172–5
- Sun J and Hynynen K 1999 The potential of transskull ultrasound therapy and surgery using the maximum available skull surface area *J. Acoust. Soc. Am.* **105** 2519–27
- Tanter M *et al* 2007 Compensating for bone interfaces and respiratory motion in high-intensity focused ultrasound *Int. J. Hyperthermia* **23** 141–51
- Tung Y S *et al* 2010 *In vivo* transcranial cavitation threshold detection during ultrasound-induced blood–brain barrier opening in mice *Phys. Med. Biol.* **55** 6141–55
- Turnbull D H and Foster F S 1991 Beam steering with pulsed two-dimensional transducer arrays *IEEE Trans. Ultrason. Ferroelect. Freq. Control* **38** 320–33
- Umemura S, Kawabata K and Sasaki K 1996 Enhancement of sonodynamic tissue damage production by second-harmonic superimposition: Theoretical analysis of its mechanism *IEEE Trans. Ultrason. Ferroelect. Freq. Control* **43** 1054–62
- Wan H, VanBaren P, Ebbini E S and Cain C A 1996 Ultrasound surgery: comparison of strategies using phased array systems *IEEE Trans. Ultrason. Ferroelect. Freq. Control* **43** 1085–98
- Yin X and Hynynen K 2005 A numerical study of transcranial focused ultrasound beam propagation at low frequency *Phys. Med. Biol.* **50** 1821–36
- Zhang D *et al* 2009 A dual-frequency excitation technique for enhancing the sub-harmonic emission from encapsulated microbubbles *Phys. Med. Biol.* **54** 4257–72